

# Multispectral Vineyard Segmentation: A Deep Learning approach

T. Barros<sup>a,\*</sup>, P. Conde<sup>a</sup>, G. Gonçalves<sup>b</sup>, C. Premebida<sup>a</sup>, M. Monteiro<sup>a</sup>, C.S.S. Ferreira<sup>c,d,e,f</sup>, U.J. Nunes<sup>a</sup>

<sup>a</sup>*Institute of Systems and Robotics, Department of Electrical and Computer Engineering, University of Coimbra, Coimbra, Portugal*

<sup>b</sup>*Institute for Systems Engineering and Computers, Department of Mathematics, University of Coimbra, Coimbra, Portugal*

<sup>c</sup>*Research Centre for Natural Resources, Environment and Society, Coimbra, Portugal*

<sup>d</sup>*Polytechnic Institute of Coimbra, Coimbra Agrarian Technical School, Coimbra, Portugal*

<sup>e</sup>*Bolin Centre for Climate Research, Department of Physical Geography, Stockholm University, Stockholm, Sweden*

<sup>f</sup>*Navarino Environmental Observatory, Navarino Dunes Messinia, Greece*

---

## Abstract

Digital agriculture has evolved significantly over the last few years due to the technological developments in automation and computational intelligence applied to the agricultural sector, including vineyards which are a relevant crop in the Mediterranean region. In this paper, a study of semantic segmentation for vine detection in real-world vineyards is presented by exploring state-of-the-art deep segmentation networks and conventional unsupervised methods. Camera data was collected on vineyards using an Unmanned Aerial System (UAS) equipped with a dual imaging sensor payload, namely a high-resolution color camera and a five-band multispectral and thermal camera. Extensive experiments of the segmentation networks and unsupervised methods have been performed on multimodal datasets representing three distinct vineyards located in the central region of Portugal. The reported results indicate that the best segmentation performances are obtained with deep networks, while traditional (non-deep) approaches using the NIR band shown competitive results. The results also show that multimodality slightly improves the performance of vine segmentation but the NIR spectrum alone generally is sufficient on most of the datasets. The code and dataset are publicly available on [https://github.com/Cybonic/DL\\_vineyard\\_segmentation\\_study.git](https://github.com/Cybonic/DL_vineyard_segmentation_study.git)

*Keywords:* Multispectral, Segmentation, Deep Learning, Remote Sensing, Vineyards, Precision Agriculture

---

## 1. INTRODUCTION

Precision agriculture has received much attention lately due to the recent technological advancements in remote sensing, mainly enabled by unmanned aerial systems (UASs) and satellites. These systems provide non-invasive, time and cost-effective techniques to automate tasks such as disease detection [1], crop yield prediction [2] and other monitoring-related tasks [3]. Conversely to satellites, which are

limited by temporal and resolution constraints, UAS-based remote sensing in the optical domain offers a cost-effective way to generate the necessary geospatial data to extract the grapevine canopy structure and its spatial variability at vineyard scale [4]. Remote sensing in combination with machine learning can be used to infer spatio-temporal variability and structure of vineyards, which are relevant for designing site-specific management strategies [5] to maximize both grape yield and quality, to avoid unnecessary treatments, and then reduce costs [6].

In terms of technology, aerial images of an onboard high-resolution RGB camera, followed by dedicated

---

\*Corresponding author

Email address: [tiagobarros@isr.uc.pt](mailto:tiagobarros@isr.uc.pt) (T. Barros)

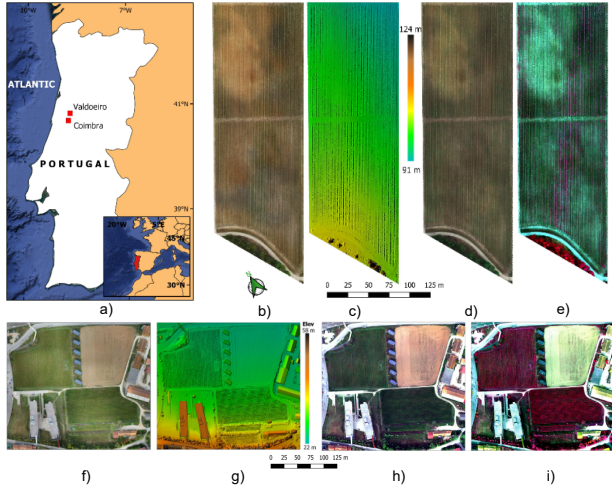


Figure 1: Study area and the corresponding Orthomosaic images - captured with an HD RGB (X7) and multispectral (Altum) cameras - considered in the datasets. a) shows the geographic locations; b), c), d) and e) show the orthomosaic images and the DSMs of the vineyard plots in Valdóeiro respectively; f), h), i) and g) correspond to the vineyard plots in Coimbra. The orthomosaics and the DSMs generated using the X7 sensor are shown in b), f) and c), g). The multispectral-based orthomosaics generated from the Altum sensor are shown in d) and h), using an R-G-B composition, while in e) and i) using false-color RE-R-G composition.

Structure-from-Motion (SfM) photogrammetric approaches is a common framework to obtain detailed (centimeter-level) Digital Surface Models (DSM) and orthomosaics of vineyards, which are often used for efficient segmentation of the grapevine canopy (see [7] and the references therein). In addition to RGB imagery, multispectral images collected by the onboard multispectral sensors comprise information from additional spectral bands such as near-infrared (NIR), red-edge (RE), and thermal (TIR), which relate to chlorophyll in green vegetation [8]. This additional information allows the measurement and mapping of the vegetation’s biochemical and biophysical attributes such as water stress and head [9, 10], crop evapotranspiration [11], biomass, or leaf pigment contents, which are key factors for vine-growers to estimate the outcomes in terms of yield and quality [12].

In vineyard-based applications, to obtain accurate prediction estimates from the aerial/UAV images we

have to concentrate on the vine plants data, while ignoring the remaining vegetation which is essential to avoid measurement contamination from undesired plants. Thus, this work resorts to image segmentation techniques to segment the pixels that contain the vine plants vs. everything else. Traditional approaches, on one hand, are based on classical (non-deep) segmentation methods which rely on handcrafted features and may have poor generalization capabilities when differentiating the background from the foreground on test data. On the other hand, deep learning (DL) segmentation approaches are end-to-end learning mechanisms that have been demonstrating exceptional performance on complex problems. One of the disadvantages, however, is linked to the presumable required amount of data to train deep models, which are scarce in many agriculture domains, particularly in vineyard-based applications.

In this work, a comprehensive study of segmentation approaches is presented for the task of vine detection in vineyard plots on both HD (high-definition) and multispectral aerial imagery collected by an UAV. The study is performed on a new dataset, that will be made public to the community, comprising UAV-based multispectral and HD-RGB orthomosaics, as well as digital surface models of vineyard plots from central Portugal, namely Coimbra and Valdóeiro regions (as shown in Fig. 1). To the best of our knowledge, this is the first dataset with such characteristics that is freely available.

The main contributions of this work are the following:

- A thorough multispectral DL-based segmentation study for vine detection in real-world vineyards;
- A new publicly available UAV-based Vineyard dataset, with annotated labels, comprising multispectral, high-resolution RGB orthomosaics, and digital surface models;
- Supervised segmentation models based on state-of-the-art deep architectures to tackle the challenging problem of semantic segmentation.

The remainder of this paper is organized as follows: Section 2 presents the state-of-the-art in the domain of semantic segmentation using UAV/drone data for precision agriculture, namely in Vineyards. In Sect. 4 the multimodal dataset, the UAV system,

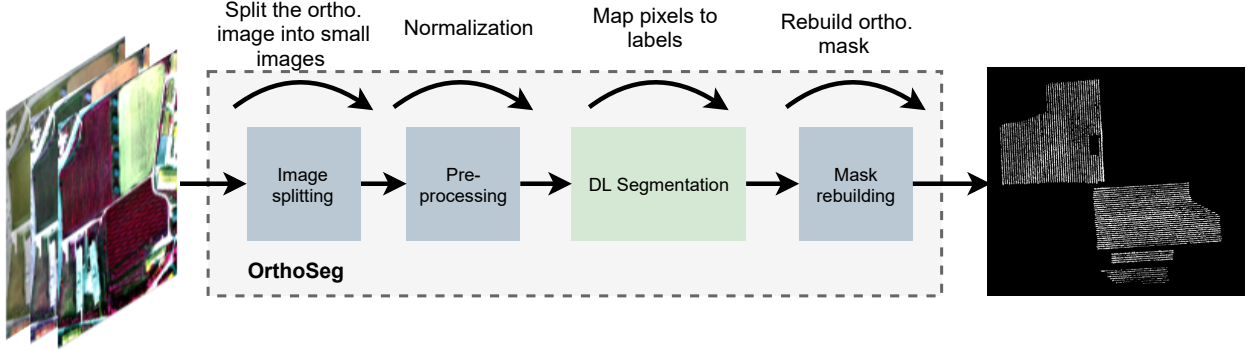


Figure 2: Orthomosaic segmentation pipeline (OrthoSeg) with the following modules: image splitting, which splits the orthomosaics into sub-images; pre-processing, which normalizes each band of the sub-images; DL segmentation, which predicts sub-masks using a DL-based segmentation approach; and mask rebuilding, which uses the sub-masks to build a mask with the same size of the input orthomosaic.

and the experimental implementation are described, while Section 5 presents and discusses the results of the experiments conducted in this work. Finally, Section 6 concludes the findings of this study and suggests future research directions.

## 2. RELATED WORK

The recent advances in drones and multispectral cameras, associated with the increasing achievements of DL-learning approaches have led to higher adoption of UAV-based multispectral imagery as a reliable information source for decision-making in agricultural tasks [2, 21, 22].

Precision agriculture and related agricultural applications have been resorting to DL approaches to perform various perception-like tasks, namely recognition, detection, and semantic segmentation - a survey on DL in agriculture can be found in [22]. Segmentation, in particular, is mainly used in this context to recognize plants or fruits from the background (soil and other residues) *e.g.*, roots from soil [23], fruits from leaves [24], or crops from weeds [25]. In vineyards, the crop plants are distinguished from weeds by detecting the rows that contain the vine plants [26].

In perception-based agricultural tasks, raw detection is a commonly used practice to avoid measurement contamination from undesired plants (*e.g.*,

weeds), which is achieved by detecting in the images the rows that contain the actual crop plants. Early row detection approaches resorted mostly to classical computer vision methods such as segmentation based on color indices [27], thresholds [28], or non-deep learning [29], which are ‘handcrafted’ approaches. Some advantages of these classical approaches comprise simplicity, ‘shallow’ training, and low computation cost. On the other hand, the disadvantages, particularly in the agriculture context, are mainly related to low performance when faced with different lighting conditions, shadows, or complex backgrounds, which makes them more suitable for simple and non-changing environments - a survey on early segmentation approaches in agriculture can be found in [21].

DL-based approaches usually rely on convolutional layers for feature learning, which enables an end-to-end data-driven approach. In [18], Convolutional Neural Networks (CNNs) are used to extract features from RGB images for row detection. That approach, called CRowNet, relies on SegNet [30] and a CNN-based Hough transform. Segmentation networks like SegNet and UNet [31] are been used in agriculture domains [14] and other applications as well (*e.g.*, urban scene segmentation [32]).

Table 1: Related work on multispectral data for semantic segmentation in digital/precision agriculture.

Ref	Bands	Fusion	Architecture/Approach	Application
[1]	RGB + NIR	Late (case-based)	Encoder-Decoder (SegNet)	Mildew disease detection in vine + row detection
[3]	RGB	Late (HSV)	Otsu's thresholding Hough Transformation	Row detection in Vineyards
[13]	RGB + NIR + RE	Early (Vegetation Indices)	Two-layer feedforward network	Vineyard water status estimation
[14]	RGB	Early (Concatenation)	Encoder-Decoder (based on Unet)	Weed/crop segmentation and classification
[15]	RGB	Early (Concatenation)	Mask R-CNN	Detection of broccoli heads
[16]	RGB + NIR + RE	Early (NDVI)	Laplacian of Gaussian unsupervised clustering random walker	Detection and segmentation of lentil plots
[17]	RGB	Early (ExG, CIVE, ExGR, VEG, ExR and ExB)	Threshold-based fuzzy clustering	Crop segmentation
[18]	RGB	Early (Concatenation)	S-SegNet HoughCNet	Crop row detection
[19]	RGB + NIR	Early (Concatenation)	Encoder-Decoder (based on SegNet)	Identification of sunflower lodging
[20]	(RGB + NIR) + DSM	Late (case-based)	Encoder-Decoder (based on SegNet)	Vine disease detection + row detection

### 3. MATERIALS AND METHODS

In vineyards, DL-based row detection can be applied to enhance vine disease detection [1, 20] or water status assessment [13], which is performed on UAS-based multispectral imagery. Using such data, on one hand, allows to capture relevant information that is not present in the RGB spectrum and, on the other hand, allows to generate DSMs from the surveyed area. In [1], the Mildew disease is detected using SegNet, which identifies regions of interest based on visible and NIR information. A similar approach is proposed in [20] where additionally to the two spectral bands, depth information is incorporated as well. A broader spectral range is used in [13] to assess the water status of vine plants, which is achieved using information from VIS, GREEN, RED, RED EDGE, and NIR, to compute vegetation indices. While the former two works (*i.e.*, [1, 20]) detect the rows through learning, the latter uses a heuristic approach that computes the height difference [33],

which is easy to implement but has limitations in areas with slopes and dense vegetation *i.e.*, tending to a poor generalization capability.

To summarise the related work on semantic segmentation applied to precision agriculture, Table 1 presents a comprehensive organization as a function of the spectral band, the fusion strategies, and the related architecture/model that have been used in this domain.

#### 3.1. Study Areas

The study was carried out in two vineyards located in the Centre of mainland Portugal, namely Valdoeiro, located in the Bairrada wine region, and Coimbra, a living-lab/farm within the Agrarian School of Coimbra (ESAC) (Fig. 1). The region has a Mediterranean climate with a strong influence of the Atlantic Ocean, characterized by average annual rainfall of 1077 mm and average annual temperature of 15 °C [34], marked by a relatively long dry summer (June-August).

Both vineyards are managed under conventional management practices but present different crop characteristics. Valdoeiro is a 2.9 ha vineyard, located at an altitude of 99 m, in flat terrain ( $< 2^\circ$ ) under Cambisol soil type, with a northeast-southwest exposure. The vineyard was planted in 2005 with a typical Baga vine variety and an approximate density of 3200 vines per ha, with plants spacing 1.3 m in straight rows and an inter-rows distance of 2.4 m. The Coimbra-ESAC vineyard extends over an area of 2.3 ha divided into two plots (*i.e.*, ESAC1 and ESAC2 see Fig. 6.a ), which are located at an altitude of 28 m, in a smoothly sloping terrain ( $2^\circ - 5^\circ$ ) under Fluvisol soil type.

The vineyard was planted in 1999 with different vine varieties such as Alfrocheiro, Aragonez, Touriga Nacional, and Marselan. ESAC1 has a south-north exposure with an approximate plant density of 2800 vines per ha, a plant distance of 1.5 m in straight rows, and an inter-rows distance of 2.4 m. ESAC2 has an east-west solar exposure with a plant density of approximately 3400 vines per ha, a plant distance of 1.4 m, and an inter-row distance of 2.1 m.

### 3.2. Materials and Data Acquisition

To survey the study areas, a compact and low-cost UAS from DJI (shown in Fig. 3) was equipped with a multispectral camera (Micasense Altum), a high-resolution (HD) RGB camera (Zenmuse X7), and a global navigation satellite systems (GNSS) with RTK correction. The UAS's flight missions were planned with the DJI Pilot 1.9 software, where the front and side overlap was set to 80% and 70%, respectively, using the Altum sensor as a reference, which captures five spectral bands (R, G, B, RE, NIR) and a thermal band. A sample of each band is illustrated in Fig. 4.

The data acquisition process was carried out by surveying both sides (*i.e.*, ESAC and Valdoeiro) with custom settings, which were set to optimize information acquisition at survey time. One of the flight settings that was adjusted was the height at which the UAS surveyed the plots. The Coimbra plots were surveyed in October at a height of 120 m after the harvest was finished. On the other hand, the Valdoeiro plot was surveyed in April. At this time, the plants are still in an early growth stage with no, or



Figure 3: UAS and the on-board cameras used for data collection.

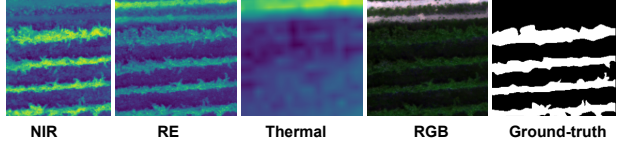


Figure 4: Image examples of the Vineyards showing the spectral bands that integrate the multispectral sensor, and a ground-truth mask.

few, visible leaves which makes plant recognition difficult at 120 m. Thus, the height was adjusted to 60 m to capture more rich and detailed information from the plants.

After data acquisition, images of both cameras were used to generate geospatial products (*i.e.*, DSM and orthomosaic) of both sites. These geospatial products were computed offline using the Structure-from-Motion (SfM) workflow available in Agisoft Metashape Professional Edition software (Agisoft LLC, St. Petersburg, Russia) version 1.7.2. The multispectral images were only used to generate orthomosaics (see Fig. 1.d, e, h and i), while HD images were used to generate both orthomosaics (see Fig. 1.b and f) and DSM (see Fig. 1.c and g). The multispectral-based orthomosaics were generated with a dedicated implementation, while the HD-based geospatial products were obtained based on a processing workflow presented in [35]. An overview of the survey conditions and of the geospatial products are presented in Table 2.

Table 2: UAS surveys and the corresponding GSD of the generated geospatial products.

Location	Date [mm/dd/yyyy]	Time [hh:mm]	Duration[min]	Weather	Flying height [m] AGL	GSD (orthomosaic) [cm/pix]		
						RGB	Multispectral	DSM
Coimbra	10/01/2020	1:40:00 pm	17	Sunny	120	1.7	4.8	3.4
Valdoeiro	04/15/2021	11:45:00 am	10	Sun/cloud	60	1	3	2

### 3.3. Orthomosaic Deep Learning-based Segmentation

Geospatial products such as orthomosaics are data structures that may have a large and arbitrary size. Such data structures are not appropriate to feed directly to DL-based approaches, which rely on CNN and are optimized for grid-based and fixed-sized inputs. Moreover, the computational demands of CNNs increase proportionally with the input size, which makes feeding orthomosaics directly to DL networks computationally too expensive. To overcome this limitation, this work resorts to an approach (named OrthoSeg illustrated in Fig. 2) that has the following steps: receives orthos as inputs; splits these orthos into sub-images; pre-processes the sub-images before being fed to the segmentation network, which outputs prediction sub-masks; and rebuilds these sub-masks into an orthomosaic mask with the same size as the initial input.

#### 3.3.1. Orthomosaic Splitting & Rebuilding

The image splitting approach has been devised to divide the orthomosaics of all bands into smaller sub-images with a fixed size of  $240 \times 240$ , which represents a much less computational burden for the DL segmentation networks.

The splitting process, as illustrated in Fig. 5, begins at the top left corner of the orthomosaic and proceeds to the right, creating sub-images every 240 pixels. After the row is completed, a new row is defined 240 pixels below. The process is repeated until the whole orthomosaic has been processed.

#### 3.3.2. Pre-processing

In order to improve convergence at training time, the generated sub-images are standardized using (1),



Figure 5: Orthomosaic splitting approach. The splitting begins at the upper left corner and proceeds to the right until the end of the row. The process is repeated until the bottom.

before being fed to the neural network,

$$X'_b = \frac{X_b - \mu_b}{\sigma_b} \quad (1)$$

where  $X_b$  represents the sub-image of the band  $b$ ,  $\mu_b$  is the mean,  $\sigma_b$  denotes the standard deviation and  $X'_b$  the corresponding standardized sub-image.

#### 3.3.3. Deep Segmentation Networks

In this work, three state-of-the-art supervised segmentation networks are used: SegNet, U-Net [31] and ModSegnet [36]. All three networks have an encoder-decoder-like architecture *i.e.*, the encoder maps the input to reduced feature space and the decoder maps the feature space to a prediction mask

with the same size as the input. The U-Net’s architecture implemented here differs slightly from the one originally proposed in [31], more specifically the network has been augmented with a Batch Normalization (BatchNorm)[37] and a Dropout layer [38], towards the goal of improving generalization and convergence.

## 4. EXPERIMENTS

The study was carried out on the proposed dataset, from which three areas of interest (AoI) were selected and are denoted by: ESAC1, ESAC2 and Valodeiro. The ground truth masks were generated in the orthomosaic space. Both the orthomosaic images and masks were processed to fit the computational requirements to train the DL-based segmentation networks, which were evaluated through a 3-fold cross-validation.

### 4.1. Dataset

All experiments were conducted on data from the 3 areas of interest: ESAC1, ESAC2, and Valodeiro, which are illustrated in Fig. 6. In Coimbra, two sets are created, which correspond to the ESAC1 and the ESAC2 plots. In Valodeiro, only the upper fraction of the plot is used, which is referred simply as Valodeiro.

For practical reasons, given the limited GPU memory available for working with images in the experiments, the three sets were divided into  $240 \times 240$  size sub-images. We note that only the images with at least 1 pixel belonging to the positive class (*i.e.*, corresponding to a vine plant) were used on the training stage.

The resulting dataset comprises thus three sets: ESAC1, ESAC2, and Valodeiro. Each set comprises data from the HD and multispectral cameras. After the splitting strategy, the HD data contains 624, 626, and 1195 images for ESAC1, ESAC2 and Valodeiro respectively; on the other hand, the multispectral data contains respectively: 85, 89, and 150 images. A summary of the dataset is presented in Table 3, where P represents the positive class (referring to vine-plants pixels) and N the negative class (referring to non vineyard pixels).

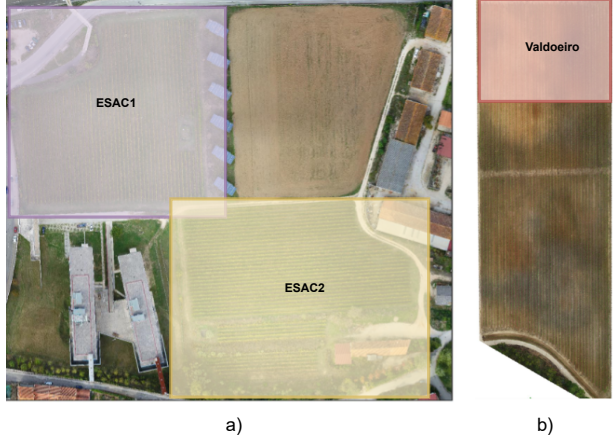


Figure 6: Areas of interest of (a) Coimbra’s vineyard plots (ESAC1 and ESAC2) and (b) Valodeiro’s plot (Valodeiro).

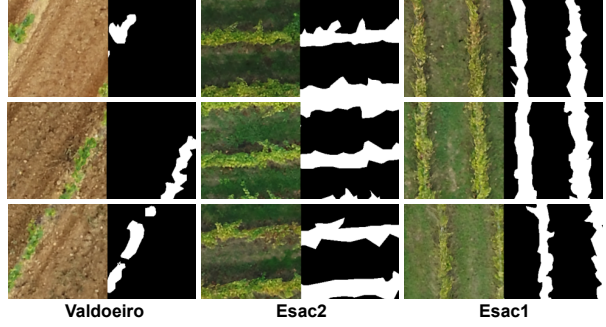


Figure 7: Sub-images and corresponding ground truth masks ( $240 \times 240$ ) used for training and testing.

### 4.2. Ground-truth data

In segmentation tasks the ground truth data correspond to masks. In this work, ground truth masks have been generated in the geospatial space (*i.e.*, orthomosaic and DSM spaces), populating the pixels that belong to vine plants with the positive class (label = 1) and the remaining pixels with a negative class (label = 0) *i.e.*, this is a binary segmentation problem. The masks were split with the same process as the orthomosaics thus, a sub-mask for each sub-image has been created. Figure 7 illustrates three sub-image samples of the three areas with their respective sub-masks, and Table 3 contains information regarding image/mask and class distributions of each

Table 3: Data and class distributions of each sensor modality where P and N represent respectively, the positive and the negative class fraction available in each set.

	I/M		HD			MS		
	MS	HD	P	N	P/N	P	N	P/N
ESAC1	85	624	0.25	0.75	3	0.23	0.77	3
ESAC2	89	626	0.28	0.72	3	0.25	0.75	3
Valdo.	150	1,196	0.07	0.93	14	0.08	0.92	12
Mean	-	-	0.17	0.83	5	0.17	0.83	5

Table 4: Image/Mask (I/M) distribution among the training and test set for cross-validation. MS denotes multispectral and HD=high-definition.

Plots	Training Set		Test Set	
	I/M		Plot	I/M
	MS	HD		
T1	ESAC1 & ESAC2	174	1250	Valdoeiro
T2	ESAC1 & Valdoeiro	235	1820	ESAC2
T3	ESAC2 & Valdoeiro	239	1822	ESAC1

area of interest.

#### 4.3. Evaluation

The evaluation procedure adopted in this work was k-fold cross-validation, using the F1-score as performance metric (2). In particular,  $k = 3$  represents the number of groups (or subsets) the dataset is split in, and corresponding to the three study areas: ESAC1, ESAC2, and Valodeiro. The three plot combinations (denoted by T1, T2, and T3) and their corresponding data distributions are represented in Table 4.

The F1 score is computed as follows,

$$F1 = \frac{2TP}{2TP + FP + FN} \quad (2)$$

where the True Positives (TP) are pixels that were correctly classified as vines; False Positives (FP) are pixels that were wrongly classified as a vine plant; True Negative (TN) are pixels that were correctly classified as background; False Negatives (FN) are pixels that were wrongly classified as background.

#### 4.4. Implementation details and Training

The implementation of this work was in a Python 3.7 environment, using for the segmentation networks the PyTorch framework. The environment was set up on a hardware with an NVIDIA GFORCE GTx1070Ti GPU and an AMD Ryzen 5 CPU with 32 GB of RAM.

All networks were initialized, trained and validated using the same conditions. The networks' weight were initialized using a normal distribution with mean 1 and a standard deviation of 0.2. The training was performed using the AdamW optimizer [39] with a learning rate and a weight decay of 0.000171 and 0.00061 respectively. The loss function was Pytorch's *BCEWithLogitsLoss* with the positive class weight set to 5 to compensate the unbalanced class distribution (as can be verified in Table 3). Data augmentation was also implemented in the form of random rotations with angles between 0 and 180 degrees, which were applied to the sub-images and the corresponding sub-masks. Finally, the networks were trained during 20 epochs, using early stopping to extract the best scores.

## 5. RESULTS AND DISCUSSION

This section reports and discusses the results obtained from the segmentation networks as well as non-deep unsupervised methods. The results in Table 5, which represent the average performance of 5 repetitions of the DL-based segmentation networks when fed with the various band combinations, were analyzed from three distinct perspectives: the network architectures, the camera been used (*i.e.*, HD vs Multispectral), and from the band configuration perspective. Additionally, comparisons have been carried out between the deep networks and the classical (non-deep) unsupervised segmentation methods.

#### 5.1. Network Comparison

Based on the reported experimental results we can deduce that the three deep networks achieved equivalent performance nonetheless, U-Net and SegNet have presented slightly higher and more 'stable' performances across the various band combinations and

Table 5: Average F1 scores of 5 repetitions. Each repetition was trained with the same parameters: 20 epochs, data augmentation, weight initialization using a normal distribution.

Sensor	Bands				SegNet				U-Net				ModSegNet						
	RGB	RE	NIR	Th.	T1	T2	T3	Mean	Std	T1	T2	T3	Mean	Std	T1	T2	T3	Mean	Std
Multispectral	×				0.73	0.78	0.79	0.77	0.03	0.73	0.76	0.82	0.77	0.04	0.72	0.77	0.77	0.75	0.02
		×			0.74	<b>0.81</b>	0.82	0.79	0.04	0.71	0.78	<b>0.85</b>	0.78	0.06	0.65	<b>0.81</b>	0.82	0.76	0.08
	×	×			0.71	0.8	0.82	0.78	0.05	0.79	0.78	0.84	0.8	0.03	0.75	<b>0.81</b>	0.82	0.79	0.03
			×		0.79	<b>0.81</b>	<b>0.83</b>	<b>0.81</b>	0.02	<b>0.81</b>	0.78	0.84	<b>0.81</b>	0.02	0.74	<b>0.81</b>	0.81	0.79	0.03
	×	×			0.79	<b>0.81</b>	<b>0.83</b>	<b>0.81</b>	0.02	0.8	<b>0.79</b>	<b>0.85</b>	<b>0.81</b>	0.03	<b>0.8</b>	0.8	0.82	<b>0.81</b>	0.01
		×	×		<b>0.8</b>	<b>0.81</b>	<b>0.83</b>	<b>0.81</b>	0.01	0.8	<b>0.79</b>	<b>0.85</b>	<b>0.81</b>	0.03	0.72	0.8	0.82	0.78	0.04
	×	×	×		0.79	<b>0.81</b>	<b>0.83</b>	<b>0.81</b>	0.02	0.8	<b>0.79</b>	<b>0.85</b>	<b>0.81</b>	0.03	0.77	0.8	<b>0.83</b>	0.8	0.02
				×	0.17	0.4	0.38	0.32	0.1	0.19	0.4	0.39	0.33	0.1	0.17	0.38	0.38	0.31	0.1
	×			×	0.74	0.77	0.78	0.76	0.02	0.71	0.76	0.82	0.76	0.04	0.75	0.76	0.74	0.75	0.01
		×		×	0.71	0.79	0.82	0.77	0.05	0.74	0.77	<b>0.85</b>	0.79	0.05	0.65	<b>0.81</b>	0.81	0.76	0.08
	×	×		×	0.72	0.8	0.82	0.78	0.04	0.74	0.78	0.84	0.79	0.04	0.74	0.8	0.81	0.78	0.03
			×	×	0.79	0.8	<b>0.83</b>	<b>0.81</b>	0.02	0.78	<b>0.79</b>	0.84	0.8	0.03	0.76	0.8	0.8	0.79	0.02
	×	×	×	×	0.78	0.8	<b>0.83</b>	0.8	0.02	0.79	<b>0.79</b>	0.84	<b>0.81</b>	0.02	<b>0.8</b>	0.79	0.81	0.8	0.01
		×	×	×	0.77	<b>0.81</b>	<b>0.83</b>	0.8	0.02	0.79	<b>0.79</b>	0.84	<b>0.81</b>	0.02	0.72	0.8	0.81	0.78	0.04
	×	×	×	×	0.76	0.8	<b>0.83</b>	0.8	0.03	<b>0.81</b>	<b>0.79</b>	0.84	<b>0.81</b>	0.02	0.78	0.8	0.82	0.8	0.02
HD	×				0.73	0.85	0.85	0.81	0.06	0.75	0.82	0.91	0.83	0.07	0.75	0.83	0.89	0.82	0.06

the train-test configurations (*i.e.*, T1, T2, and T3). Despite the seasonal change of the vineyards, the networks demonstrated high generalization capability.

### 5.2. HD vs Multispectral

When comparing the scores w.r.t. the sensor perspective (*i.e.*, HD RGB vs multispectral modalities), HD-based F1-scores are in general higher, which can be partially explained by a larger amount of training data available *i.e.*, largest amount of pixels due to higher resolution (see Table 4 for the number of images in each dataset). Nonetheless, when focusing on the T1 scenario, where the networks are trained in a completely different scenario from which they are tested, it is interesting to observe how the multispectral modalities allow a better overall performance.

### 5.3. Spectral Band Comparison

From the results, one key observation is notable: the NIR spectral band tends to generate the best

results thus, using this band alone is sufficient to achieve proficient results. In some cases adding other bands does not improve but, even downgrades the performances. The thermal band is one of such cases, having very low performance when used alone. A possible reason behind the thermal-band having such poor outcome is due to its low resolution when compared with the other bands (see Fig. 4).

Despite the high performance of the NIR band, having access to such information requires multispectral cameras, which are less affordable than their RGB counterparts. Thus, due to the low cost and ease of acquiring, color cameras are very popular among the works in agriculture (as can be seen in Table 1). Comparing the results of the RGB band with the best-performing band combination, RGB has on average 4% lower performance, which is acceptable when a multispectral camera is not an option.

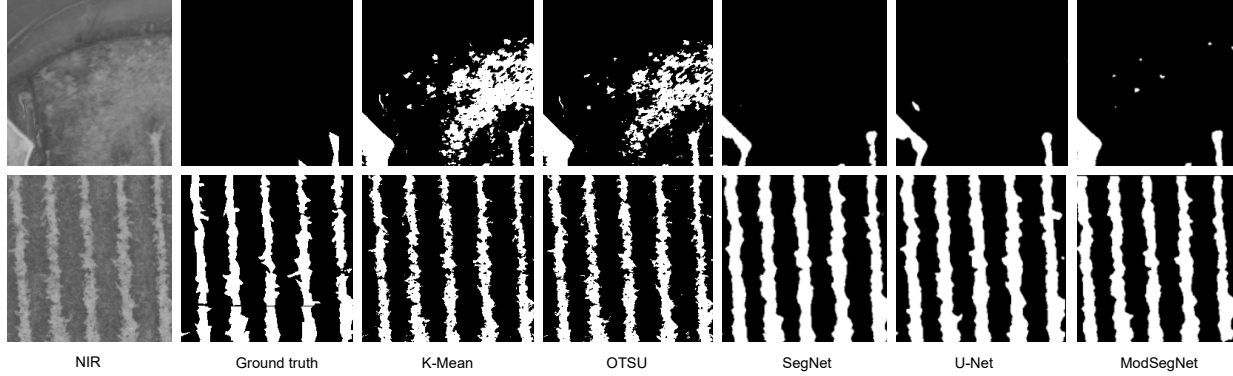


Figure 8: Qualitative prediction masks comparison of DL-based and classical approaches. The two samples represent: (upper) a corner-case where classical approaches have low performance; and (lower) an ideal case where classical approaches are competitive with DL-based approaches.

#### 5.4. Deep vs Conventional Unsupervised Methods

For the sake of comparison with the DL segmentation networks, two unsupervised methods of image segmentation (OTSU and K-means) were used in some of the previously tested modalities (RGB-HD, RGB, RE, and NIR). The methods were independently applied in the selected regions (ESAC1, ESAC2, and Valdoeiro) in an unsupervised fashion and evaluated against the ground truth. For the K-means method, the same type of band-wise normalization (used in our previous Deep Learning methods) has been applied during the pre-processing phase.

Analogous to the deep methods, also here the NIR band led to the highest F1-scores. Overall, the unsupervised methods achieved unsatisfactory segmentation performances, with many F1 scores below 0.50. Nonetheless, when using the NIR band, competitive results are attained across the different regions of the dataset as shown in Table 6 which presents a comparison of both DL and non-deep methods using the NIR band. We can see that the best DL networks outperformed 6 point-percentage in average the non-deep methods. Additionally, we note that the ‘shallow’ methods struggle in some corner cases where the positive class is scarce, contrarily to DL-based approaches (as illustrated in Fig. 8).

Table 6: Segmentation performance (F1 scores) of the unsupervised (non-deep) and the deep networks using the NIR band.

	Valdoeiro	ESAC1	ESAC2	Mean
OSTSU	0.78	0.78	0.70	0.75
K-Mean	0.78	0.78	0.70	0.75
SegNet	0.79	0.83	<b>0.81</b>	<b>0.81</b>
U-Net	<b>0.81</b>	<b>0.84</b>	0.78	<b>0.81</b>
ModSegNet	0.74	0.81	<b>0.81</b>	0.79

## 6. CONCLUSIONS

In this work, a new UAV-based multispectral and HD RGB dataset has been used to train three deep segmentation networks for the task of pixel-wise vineyard recognition. The aim was to study the responses of the different spectral bands, image resolutions, and segmentation networks when used in this agricultural application. The data was captured from two distinct vineyards at different seasonal stages, both located in the central region of Portugal: Coimbra and Valdoeiro.

From the results of this study, two major conclusions are derived. Firstly, the higher image resolution in the HD RGB modality increases the general performance of the DL networks, when compared with the different multispectral modalities, but is not

sufficient when we restrain our analysis to the scenario of greater generalization (illustrated by the T1 data configuration). Secondly, focusing on the performance of different bands from the multispectral camera, the NIR band stands out not only as ubiquitous in the best performing combinations, but even for the robust results that are possible to obtain when used as a single modality. The latter observation was further substantiated when conventional unsupervised segmentation methods were compared with our DL-network architectures; in this scenario, competitive results were only possible when the conventional algorithms were applied to the NIR band, despite the problems in some corner cases.

The present article makes a good case for the use of this type of dual-camera approach to UAV-based data acquisition, highlighting the clear advantages and disadvantages of each option and discussing, in a thorough and rigorous way, the best semantic segmentation approaches for each scenario. Finally, the DL-based networks were compared with traditional approaches, underlining the importance of this type of study for real-life precision agriculture applications. For future work, a combination of data acquired from both cameras could be introduced in our analysis of Neural Network performance, as well as some depth information retrieved from the DSMs.

## ACKNOWLEDGMENTS

This work has been supported by the Portuguese Foundation for Science and Technology (FCT) via the projects AI+Green (MIT-EXPL/TDI/0029/2019) and Agribotics (UIDB/00048/2020). The work of G. Gonçalves was also supported by the FCT through the grant UIDB/00308/2020.

## References

- [1] M. Kerkech, A. Hafiane, R. Canals, Vine disease detection in uav multispectral images using optimized image registration and deep learning segmentation approach, *Computers and Electronics in Agriculture* 174 (2020) 105446. doi:<https://doi.org/10.1016/j.compag.2020.105446>.
- [2] T. van Klompenburg, A. Kassahun, C. Catal, Crop yield prediction using machine learning: A systematic literature review, *Computers and Electronics in Agriculture* 177 (2020) 105709. doi:<https://doi.org/10.1016/j.compag.2020.105709>.
- [3] G. D. Karatzinis, S. D. Apostolidis, A. C. Kapoutsis, L. Panagiotopoulou, Y. S. Boutalis, E. B. Kosmatopoulos, Towards an integrated low-cost agricultural monitoring system with unmanned aircraft system (2020) 1131–1138. doi:[10.1109/ICUAS48674.2020.9213900](https://doi.org/10.1109/ICUAS48674.2020.9213900).
- [4] L. Deng, Z. Mao, X. Li, Z. Hu, F. Duan, Y. Yan, UAV-based multispectral remote sensing for precision agriculture: A comparison between different cameras, *ISPRS Journal of Photogrammetry and Remote Sensing* 146 (2018) 124–136. doi:[10.1016/j.isprsjprs.2018.09.008](https://doi.org/10.1016/j.isprsjprs.2018.09.008).
- [5] A. I. de Castro, F. M. Jiménez-Brenes, J. Torres-Sánchez, J. M. Peña, I. Borra-Serrano, F. López-Granados, 3-D Characterization of Vineyards Using a Novel UAV Imagery-Based OBIA Procedure for Precision Viticulture Applications, *Remote Sensing* 10 (2018) 584. doi:[10.3390/rs10040584](https://doi.org/10.3390/rs10040584).
- [6] L. Pádua, T. Adão, A. Sousa, E. Peres, J. J. Sousa, Individual Grapevine Analysis in a Multi-Temporal Context Using UAV-Based Multi-Sensor Imagery, *Remote Sensing* 12 (2020) 139. doi:[10.3390/rs12010139](https://doi.org/10.3390/rs12010139).
- [7] L. Pádua, P. Marques, J. Hruška, T. Adão, J. Bessa, A. Sousa, E. Peres, R. Morais, J. J. Sousa, Vineyard properties extraction combining UAS-based RGB imagery with elevation data, *International Journal of Remote Sensing* 39 (2018) 5377–5401. doi:[10.1080/01431161.2018.1471548](https://doi.org/10.1080/01431161.2018.1471548).
- [8] J. Xue, B. Su, Significant remote sensing vegetation indices: A review of developments and applications, *Journal of sensors* 2017 (2017).

[9] J. Costa, M. Vaz, J. Escalona, R. Egipto, C. Lopes, H. Medrano, M. Chaves, Modern viticulture in southern europe: Vulnerabilities and strategies for adaptation to water scarcity, *Agricultural Water Management* 164 (2016) 5–18. doi:<https://doi.org/10.1016/j.agwat.2015.08.021>, enhancing plant water use efficiency to meet future food production.

[10] I. Pôcas, A. Rodrigues, S. Gonçalves, P. M. Costa, I. Gonçalves, L. S. Pereira, M. Cunha, Predicting grapevine water status based on hyperspectral reflectance vegetation indices, *Remote Sensing* 7 (2015) 16460–16479. doi:[10.3390/rs71215835](https://doi.org/10.3390/rs71215835).

[11] M. Ferreira, N. Conceição, J. Silvestre, M. Fabião, et al., Transpiration and water stress effects on water use, in relation to estimations from ndvi: application in a vineyard in se portugal, *Options Méditerranéennes: Série B. Etudes et Recherches* (2012) 203–208.

[12] Comparison of Satellite and UAV-Based Multispectral Imagery for Vineyard Variability Assessment, *Remote Sensing* 11 (2019) 436.

[13] M. Romero, Y. Luo, B. Su, S. Fuentes, Vineyard water status estimation using multispectral imagery from an uav platform and machine learning algorithms for irrigation scheduling management, *Computers and electronics in agriculture* 147 (2018) 109–117.

[14] M. Fawakherji, A. Youssef, D. Bloisi, A. Pretto, D. Nardi, Crop and weeds classification for precision agriculture using context-independent pixel-wise segmentation, in: 2019 Third IEEE International Conference on Robotic Computing (IRC), IEEE, 2019, pp. 146–152.

[15] P. M. Blok, F. K. van Evert, A. P. Tielen, E. J. van Henten, G. Kootstra, The effect of data augmentation and network simplification on the image-based detection of broccoli heads with mask r-cnn, *Journal of Field Robotics* 38 (2021) 85–104.

[16] I. Ahmed, M. Eramian, I. Ovsyannikov, W. van der Kamp, K. Nielsen, H. S. Duddu, A. Rumali, S. Shirtliffe, K. Bett, Automatic detection and segmentation of lentil crop breeding plots from multi-spectral images captured by uav-mounted camera, in: 2019 IEEE Winter Conference on Applications of Computer Vision (WACV), IEEE, 2019, pp. 1673–1681.

[17] M. Guijarro, G. Pajares, I. Riomoros, P. Herrera, X. Burgos-Artizzu, A. Ribeiro, Automatic segmentation of relevant textures in agricultural images, *Computers and Electronics in Agriculture* 75 (2011) 75–83.

[18] M. D. Bah, A. Hafiane, R. Canals, Crownet: Deep network for crop row detection in uav images, *IEEE Access* 8 (2019) 5189–5200.

[19] Z. Song, Z. Zhang, S. Yang, D. Ding, J. Ning, Identifying sunflower lodging based on image fusion and deep semantic segmentation with uav remote sensing imaging, *Computers and Electronics in Agriculture* 179 (2020) 105812.

[20] M. Kerkech, A. Hafiane, R. Canals, F. Ros, Vine disease detection by deep learning method combined with 3d depth information, in: International Conference on Image and Signal Processing, Springer, 2020, pp. 82–90.

[21] E. Hamuda, M. Glavin, E. Jones, A survey of image processing techniques for plant extraction and segmentation in the field, *Computers and Electronics in Agriculture* 125 (2016) 184–199. doi:<https://doi.org/10.1016/j.compag.2016.04.024>.

[22] A. Kamilaris, F. X. Prenafeta-Boldú, Deep learning in agriculture: A survey, *Computers and Electronics in Agriculture* 147 (2018) 70–90. doi:<https://doi.org/10.1016/j.compag.2018.02.016>.

[23] C. Douarre, R. Schielein, C. Frindel, S. Gerth, D. Rousseau, Deep learning based root-soil segmentation from x-ray tomography images, *bioRxiv* (2016) 071662.

[24] S. Bargoti, J. P. Underwood, Image segmentation for fruit detection and yield estimation in apple orchards, *Journal of Field Robotics* 34 (2017) 1039–1060.

[25] S. Haug, J. Ostermann, A crop/weed field image dataset for the evaluation of computer vision based precision agriculture tasks, in: European conference on computer vision, Springer, 2014, pp. 105–116.

[26] M. D. Bah, A. Hafiane, R. Canals, CRowNet: Deep network for crop row detection in uav images, *IEEE Access* 8 (2020) 5189–5200. doi:10.1109/ACCESS.2019.2960873.

[27] K. Kirk, H. J. Andersen, A. G. Thomsen, J. R. Jørgensen, R. N. Jørgensen, Estimation of leaf area index in cereal crops using red–green images, *Biosystems Engineering* 104 (2009) 308–317.

[28] H. Y. Jeon, L. F. Tian, H. Zhu, Robust crop and weed segmentation under uncontrolled outdoor illumination, *Sensors* 11 (2011) 6270–6283.

[29] J. M. Guerrero, G. Pajares, M. Montalvo, J. Romeo, M. Guijarro, Support vector machines for crop/weeds identification in maize fields, *Expert Systems with Applications* 39 (2012) 11149–11155.

[30] V. Badrinarayanan, A. Kendall, R. Cipolla, Segnet: A deep convolutional encoder-decoder architecture for image segmentation, *IEEE transactions on pattern analysis and machine intelligence* 39 (2017) 2481–2495.

[31] O. Ronneberger, P. Fischer, T. Brox, U-net: Convolutional networks for biomedical image segmentation, in: International Conference on Medical image computing and computer-assisted intervention, Springer, 2015, pp. 234–241.

[32] D. Hong, J. Yao, D. Meng, Z. Xu, J. Chanussot, Multimodal gans: Toward crossmodal hyperspectral–multispectral image segmentation, *IEEE Transactions on Geoscience and Remote Sensing* 59 (2020) 5103–5113.

[33] S. Baofeng, X. Jinru, X. Chunyu, S. Yuyang, S. Fuentes, et al., Digital surface model applied to unmanned aerial vehicle based photogrammetry to assess potential biotic or abiotic effects on grapevine canopies, *International Journal of Agricultural and Biological Engineering* 9 (2016) 119–130.

[34] C. Ferreira, J. Keizer, L. Santos, D. Serpa, V. Silva, M. Cerqueira, A. Ferreira, N. Abrantes, Runoff, sediment and nutrient exports from a mediterranean vineyard under integrated production: An experiment at plot scale, *Agriculture, Ecosystems & Environment* 256 (2018) 184–193.

[35] G. Gonçalves, D. Gonçalves, Á. Gómez-Gutiérrez, U. Andriolo, J. A. Pérez-Alvárez, 3D Reconstruction of Coastal Cliffs from Fixed-Wing and Multi-Rotor UAS: Impact of SfM-MVS Processing Parameters, Image Redundancy and Acquisition Geometry, *Remote Sensing* 13 (2021) 1222. doi:10.3390/rs13061222.

[36] P.-A. Ganaye, M. Sdiha, H. Benoit-Cattin, Semi-supervised learning for segmentation under semantic constraint, in: International Conference on Medical Image Computing and Computer-Assisted Intervention, Springer, 2018, pp. 595–602.

[37] S. Ioffe, C. Szegedy, Batch normalization: Accelerating deep network training by reducing internal covariate shift, in: International conference on machine learning, PMLR, 2015, pp. 448–456.

[38] N. Srivastava, G. Hinton, A. Krizhevsky, I. Sutskever, R. Salakhutdinov, Dropout: a simple way to prevent neural networks from overfitting, *The journal of machine learning research* 15 (2014) 1929–1958.

[39] I. Loshchilov, F. Hutter, Decoupled weight decay regularization, in: International Conference on Learning Representations, 2019.